

A study of iso- and alio-valent cation doped Ag_2SO_4 solid electrolyte

K. Singh¹, S.M. Pande², S.W. Anwane³, S.S. Bhoga³

¹Department of Physics, Amravati University, Amravati-444 602, India

²Department of Physics, Shri R.K.N. Engineering College, Gittikhadan, Katol Road, Nagpur-440 013, India

³Department of Physics, Nagpur University, Nagpur-440 010, India

Received: 3 February 1997/Accepted: 27 May 1997

Abstract. AC conductivity results are obtained by incorporating various guest iso-valent and alio-valent cations within the solid solubility limit with different ionic radii in both the structural modifications of Ag_2SO_4 . The solid solubility limits up to $x \leq 3$ mole% for monovalent, $x \leq 5.27$ mole% for divalent and $x \leq 3.63$ mole% for trivalent cation doped Ag_2SO_4 are set with XRD, SEM, IR and DSC techniques. A predominant dependence of conductivity on the ionic size of iso- and alio-valent cations is observed. In particular, the conductivity enhances in both α and β phases, despite having a lower ionic-size dopant cation (relative to that of Ag^+) in the transition element cation doped Ag_2SO_4 . Ca^{2+} , Ba^{2+} , Y^{3+} and Dy^{3+} doped samples show departure from the regular behaviour in the β -phase. The conductivity behaviour is discussed considering ionic size, valence and electronic structure of the guest cations.

PACS: 66.30; 61.7; 82.45

Amongst all sulphate-based solid electrolytes, silver sulphate, a non-alkali metal sulphate, is an exception which shows high cationic conductivity in spite of the bigger size of Ag^+ (1.26 Å). It undergoes a phase transition from the high-temperature highly conducting hexagonal α -phase to the low-temperature moderately conducting orthorhombic β -phase at 416 °C. It attracted scant attention till its potential application in SO_x galvanic sensors was proved [1]. Recently, ever since the concept of using a metal/metal sulphate reference electrode in solid electrochemical gas sensors evolved, it has attracted a great deal of attention. It exhibits many advantages over other sulphate-based solid electrolytes in engineering SO_2 gas sensors like: (i) coexistence of Ag–O–S phase in Ag/ Ag_2SO_4 ; (ii) equilibration of antagonist SO_4^{2-} (solid) with SO_2/SO_3 (gas); (iii) invariance of high ionic conductivity over the SO_x environment, etc. [2–4].

In contrast to earlier reports [5], our preliminary investigations reveal that in addition to valence, the ionic size and electronic structure of doped cations do play an important role in ion transport through the solid in low-temperature phases of sulphates [6–9]. The present work attempts a systematic and

in-depth study on the influence of lattice distortion and role of electronic structure caused by iso-valent and alio-valent (d-block, s-block and rare-earth cations) on Ag^+ mobility in hexagonal α - and orthorhombic β - Ag_2SO_4 to understand the fundamental conduction mechanism and simultaneously to obtain an apt silver sulphate based material for SO_2 gas sensor.

1 Experimental

The initial ingredients Ag_2SO_4 , Me_2SO_4 , MSO_4 and $\text{M}'_2(\text{SO}_4)_3$ (where Me = Li, Na, K, Rb, Cs; M = Co, Ni, Mn, Mg, Cu, Ca, Ba, Zn, Pb, Sr, and M' = La, Y, Dy, Sm, Gd) with assay more than 99.99% were procured from Aldrich Chemicals (USA). These pre-dried initial ingredients with mole fractions $(100-x)\text{Ag}_2\text{SO}_4:(x)\text{Me}_2\text{SO}_4$ (where $x = 0-7$), $(100-x)\text{Ag}_2\text{SO}_4:(x)\text{MSO}_4$ and $(100-x)\text{Ag}_2\text{SO}_4:(x)\text{M}'_2(\text{SO}_4)_3$ (where $x = 0-10$) were mixed in an agate mortar under acetone for 2 h. The compositions were filled in translucent quartz ampules (to avoid photo decomposition of Ag_2SO_4) and were heated in an electric furnace to a temperature 20 °C above the melting-point. Later, the melt was allowed to crystallize by cooling at a cooling rate of 1.5 °C min⁻¹. The ingots obtained by breaking the ampules were pulverized to get a fine powder. The prepared samples were characterized by X-ray powder diffraction (XRD) (Philips PW 1700 diffractometer attached with PW 1710 controlling unit) using CuK_α radiation. The solid–solid phase transition temperature and the heat of transition were studied by differential scanning calorimetry (DSC) using Mettler TA 4000, DSC 25 at a heating rate of 10 °C min⁻¹. The microstructures were examined with the help of scanning electron microscope (SEM) (Cambridge 250 Mark-III stereoscan electron microscope). Using infrared (IR) spectroscopy, the stack plots of the samples were recorded in several spectral regions of interest using a Perkin-Elmer 983 IR spectrometer.

For electrical characterization, the specimens were obtained in the form of circular discs of 9 mm diameter and 2 mm thickness by pressing the powder with the help of a Specac (UK) stainless steel die-punch and hydraulic press.

The pellets so obtained were sintered at 500 °C for 24 h. Prior to spring loading of the pellets between silver electrodes, a good ohmic contact was ensured by using a quality silver paint on both opposite parallel surfaces of the pellet, followed by baking at 200 °C for 2 h. Preceding the impedance measurement, the spring-loaded sample was heated to 510 °C for an hour to homogenize the charge carriers in the sample and simultaneously to remove the moisture content therein. Later, the temperature of the furnace was reduced in step of 20 °C at a cooling rate of 2 °C min⁻¹. At the end of each cycle the sample was allowed to attain thermal equilibrium for a dwell time of 30 minutes using a Eurotherm 810 PID temperature controller. At the end of each dwell time, the real and imaginary parts of the impedance were measured as parametric functions of frequency in the range 5 Hz–13 MHz and temperatures from 510 to 100 °C during the cooling cycle using an HP 4192A IF impedance analyser. The entire measurement system was properly shielded to avoid external electrical pickups. The reproducibility of the impedance data was confirmed by repeating the measurement on freshly prepared samples. The ionic transference number of the specimens was measured by Wagner's dc polarization method using a Keithley SMU 236 with cell configuration:

Ag/Electrolyte/Pt

2 Results and discussion

Structural characterization forms the very basis for understanding the structure correlated conduction mechanism.

Table 1. A comparison of the experimental d and I/I_0 values with JCPDS data for (97)Ag₂SO₄ : (3)Me₂SO₄

Me = Li		Me = Na		Me = Rb		Me = Cs		JCPDS		[hkl]	Phase
$d(\text{Å})$	I/I_0										
4.694	7	4.702	8	4.698	7	–	–	4.699	10	[111]	β-Ag ₂ SO ₄
3.987	20	3.985	11	3.995	20	–	–	3.994	25	[220]	β-Ag ₂ SO ₄
3.171	59	3.171	29	3.178	68	3.177	59	3.177	70	[040]	β-Ag ₂ SO ₄
2.871	100	2.873	100	2.875	100	2.878	100	2.873	100	[311]	β-Ag ₂ SO ₄
2.642	48	2.648	31	2.646	54	2.647	55	2.644	90	[022]	β-Ag ₂ SO ₄
2.415	23	2.418	12	2.421	24	2.425	32	2.421	30	[311]	β-Ag ₂ SO ₄
1.926	17	1.923	18	1.927	26	–	–	1.926	30	[351]	β-Ag ₂ SO ₄
1.708	14	1.713	8	1.711	19	–	–	1.712	17	[062]	β-Ag ₂ SO ₄

Table 2. A comparison of the experimental d and I/I_0 values with JCPDS data for (94.73)Ag₂SO₄ : (5.27)MSO₄, and (96.37)Ag₂SO₄ : (3.63)(M'₂SO₄)₃

M = Co		M = Cu		M = Mn		M = Ni		M = Mg		M = Sr		M = Ba		M' = La		JCPDS		[hkl]	Phase
$d(\text{Å})$	I/I_0																		
4.704	8	4.706	10	4.722	9	–	–	4.697	10	4.709	6	4.711	9	4.718	0	4.699	10	[111]	β-Ag ₂ SO ₄
3.997	15	3.997	20	4.013	21	4.016	24	3.998	16	4.001	14	4.018	23	4.006	10	3.994	25	[220]	β-Ag ₂ SO ₄
3.175	56	3.177	48	3.184	75	3.179	77	3.175	62	3.179	41	3.179	50	3.184	46	3.177	70	[040]	β-Ag ₂ SO ₄
2.879	100	2.877	100	2.881	100	2.895	100	2.875	100	2.878	100	2.879	100	2.875	100	2.873	100	[311]	β-Ag ₂ SO ₄
2.647	40	2.645	37	2.653	64	2.641	19	2.648	45	2.647	40	2.652	43	2.659	20	2.644	90	[022]	β-Ag ₂ SO ₄
2.533	12	2.535	6	2.538	18	2.542	26	2.530	15	2.533	5	2.535	16	–	–	2.53	17	[400]	β-Ag ₂ SO ₄
2.424	20	2.423	15	2.431	18	2.43	29	2.421	15	2.422	14	2.428	20	2.425	18	2.421	20	[331]	β-Ag ₂ SO ₄
1.926	19	1.927	18	1.928	24	–	–	1.927	22	1.926	16	1.929	21	1.925	14	1.926	30	[351]	β-Ag ₂ SO ₄
1.915	8	1.915	11	1.917	10	1.918	22	–	–	–	–	–	–	–	–	1.915	12	[511]	β-Ag ₂ SO ₄
1.712	12	1.713	11	1.714	16	1.719	18	1.713	11	1.714	8	–	–	–	–	1.712	17	[062]	β-Ag ₂ SO ₄
1.672	12	1.672	8	1.676	17	–	–	1.675	10	–	–	–	–	–	–	1.673	12	[313]	β-Ag ₂ SO ₄
1.567	9	1.568	9	–	–	–	–	1.566	9	–	–	–	–	–	–	1.567	13	[333]	β-Ag ₂ SO ₄
1.546	7	1.546	8	1.546	9	1.549	9	1.544	7	1.547	7	1.549	10	–	–	1.546	8	[371]	β-Ag ₂ SO ₄

β-Ag₂SO₄ → JCPDS file No. 27-1403 Orthorhombic β-Ag₂SO₄

2.1 X-ray powder diffraction

A comparison of experimental, d , and relative intensity values, I/I_0 , with those of JCPDS data is given in Tables 1, 2. It is clearly evident that in the case of 3 mole% Me₂SO₄ added to Ag₂SO₄ the d values in XRD patterns are slightly deviated from the JCPDS data of β-Ag₂SO₄ (Table 1). This small deviation in experimental $d(\text{Å})$ values can be attributed to the partial replacement of Ag⁺ by wrong-size Me⁺. Further, no decomposition appears from the XRD data. The absence of any line corresponding to either Me₂SO₄, AgMeSO₄ or any other intermediate phase for 3 mole% Me₂SO₄ added to Ag₂SO₄ indicates solid solubility (SS). The appearance of few meagre lines corresponding to Me₂SO₄ in the case of (95) Ag₂SO₄:(5) Me₂SO₄ added to Ag₂SO₄ indicates the advent of precipitation following its *in situ* dispersion in the host Ag₂SO₄(SS). A closer look at Table 1 reveals that, in general, there is a slight shift (negative) in $d(\text{Å})$ values for the systems where the dopant ion size is smaller than that of Ag⁺, such as Li⁺ and Na⁺, whereas the shift is positive in $d(\text{Å})$ values for dopants with relatively bigger-size cations, such as K⁺, Rb⁺ and Cs⁺. Using a similar procedure, the solid solubility limits for MSO₄ and M'₂(SO₄)₃ doped Ag₂SO₄ are found to be $x \leq 52.7$ and $x \leq 3.63$, respectively.

The local lattice distortion caused by the 'wrong'-size cation substitutions was further investigated to detect the magnitude of the distortion. A closer look at Table 3 reveals that the cell volume undergoes a continuous contraction for Na⁺ and Li⁺; whereas it undergoes a continuous expansion for K⁺, Rb⁺ and Cs⁺ substitution. These results (lattice contraction/expansion on the substitution of the

Table 3. Lattice constants and cell volume of (97)Ag₂SO₄ : (3)Me₂SO₄, (94.73)Ag₂SO₄ : (5.27)MSO₄, and (96.37)Ag₂SO₄ : (3.63)(M'₂SO₄)₃ systems

Cell constant (Å)	Me = Li	Me = Na	Me = Rb	Me = Cs	M = Co	M = Cu	M = Mn	M = Ni	M = La	JCPDS
<i>a</i>	10.221	10.227	10.241	10.267	10.252	10.249	10.258	10.251	10.255	10.269
<i>b</i>	12.682	12.686	12.714	12.737	12.684	12.683	12.694	12.688	12.704	12.706
<i>c</i>	5.753	5.750	5.853	5.841	5.804	5.800	5.809	5.817	5.811	5.818
Cell Volume (Å) ³	745.87	746.18	764.20	766.92	754.73	753.93	756.42	756.58	757.05	759.25

smaller/bigger alio-valent cations (Table 3)) are suggestive of the fact that lattice distortion (expansion and contraction) is directly governed by the 'distortion factor', $r_g - r_h$, r_g and r_h being the ionic radii of the guest and host cations, respectively. Figure 1 displays the variation of d_{100} (d value for 100% characteristic line) with the lattice distortion factor, $r_g - r_h$, at a fixed dopant concentration, $x = 3$ mole%, and ambient temperature for all the series. As seen, the d_{100} values of all the doped samples are almost invariant over the distortion factor, except for the Y³⁺, Dy³⁺ and Ca²⁺ doped samples for which there is a dramatic deviation of d_{100} value to the lower side. This does indicate some anomaly with respect to the modified structure of the lattice upon doping at least in these samples.

2.2 Scanning electron microscopy (SEM)

The grain morphology of the host material is more or less unaffected by the addition of up to 3.63 mole% (Figs 2a–c), whereas traces of a second precipitated phase are visible for samples with 4.72 mole% La₂(SO₄)₃ in Ag₂SO₄. Similar results are found for other monovalent sulphate added to Ag₂SO₄ systems. These results suggest that a complete solid solution can be ensured up to 3 mole% of Me₂SO₄ in Ag₂SO₄

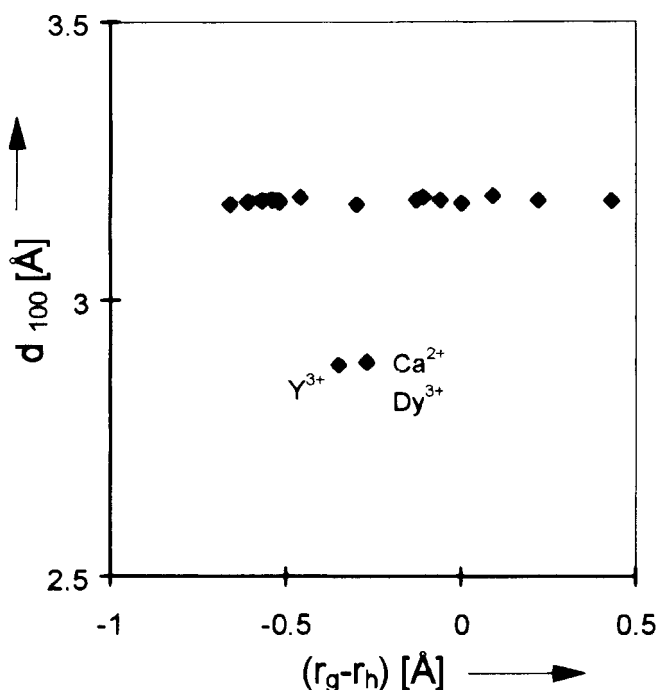


Fig. 1. Variation of d_{100} with $r_g - r_h$ for 3 mole% of mono-, di- and trivalent cation doped Ag₂SO₄

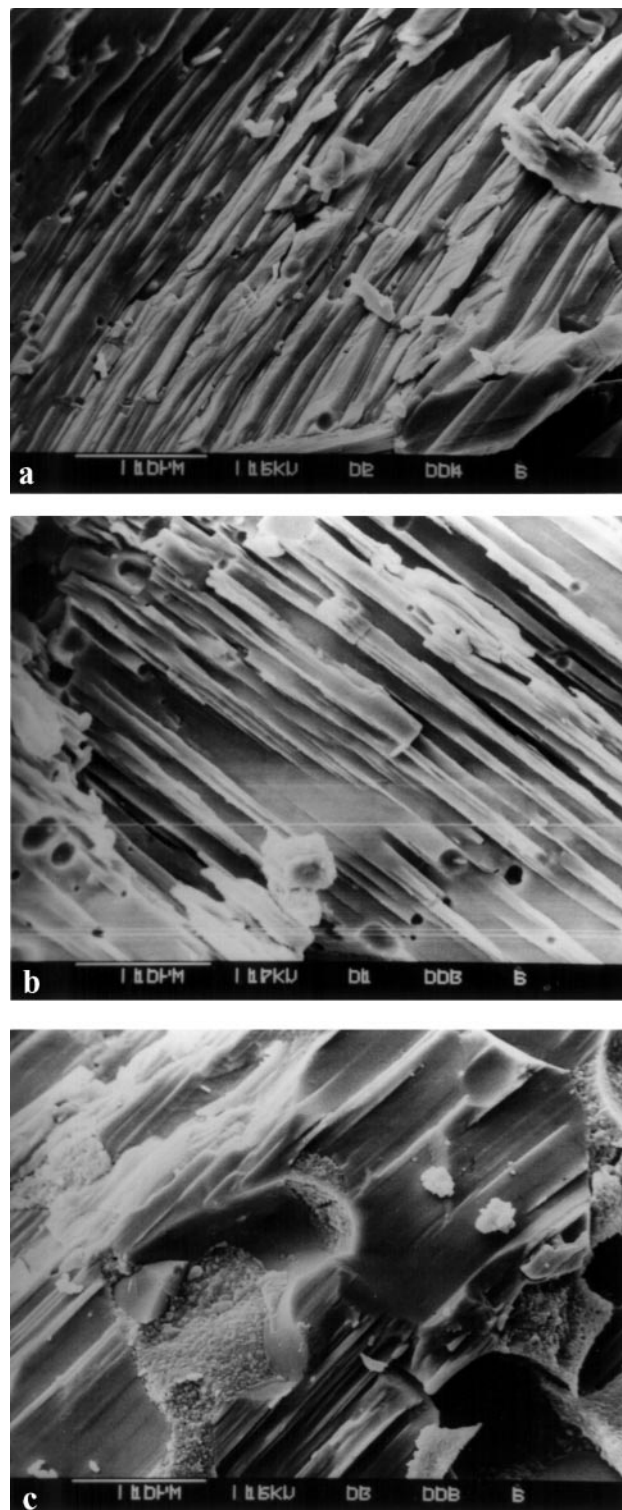


Fig. 2. Microphotographs for $x \leq 3.63$ in La³⁺ doped Ag₂SO₄

at room temperature. Similarly, on the same lines the solid solubility is ensured up to $x \leq 5.27$ and $x \leq 3.63$ in cases of di- and trivalent cation doped Ag_2SO_4 , respectively. These results are in good agreement with XRD analysis.

2.3 Differential scanning calorimetry (DSC)

Figure 3a shows the variations of the solid–solid phase transition temperature (T_c) and transition enthalpy (ΔH) with the MnSO_4 concentration in Ag_2SO_4 . T_c is seen decreasing at a faster rate with impurity concentration up to $x \leq 5.27$ mole%, after which it further decreases with a moderate rate to a value of about 409°C . On the other hand, ΔH increases with dopant concentration ($x \leq 5.27$ mole%) and falls off upon further addition. No additional peaks were observed apart from that at $T_c \sim 419^\circ\text{C}$ which rules out the possi-

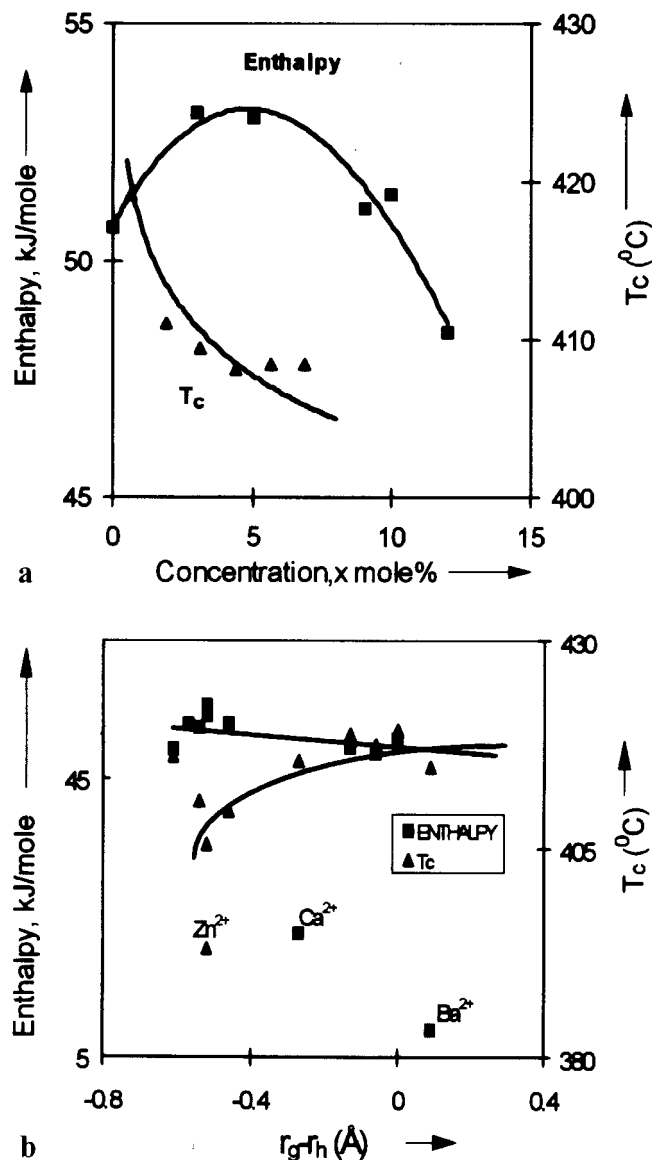


Fig. 3. Variations of transition temperature (T_c) and enthalpy of transition (ΔH) with (a) concentration for the $(100-x)\text{Ag}_2\text{SO}_4 : (x)\text{MnSO}_4$ system and (b) distortion factor ($r_g - r_h$) for $(100-x)\text{Ag}_2\text{SO}_4 : (x)\text{MSO}_4$ system

bility of formation of any other intermediate phase. An exceptional case is that of $(100-x)\text{Ag}_2\text{SO}_4 : (x)\text{ZnSO}_4$ (where $x = 3.12, 5.27$ and 10) which shows a doublet having a weak peak at $T_c \sim 358^\circ\text{C}$. Since ZnSO_4 decomposes at 600°C during the course of sample preparation, they are discarded from further study. The variation of T_c with $r_g - r_h$ is shown in Fig. 3b. As seen, except for Pb^{2+} and Zn^{2+} doped samples, the transition temperature, in general, is lower than that of the host ($T_c \sim 419^\circ\text{C}$). It is worth mentioning that Pb^{2+} , on account of possessing exceptionally high polarizability, is known for its anomalous behaviour, whereas Zn^{2+} doped samples show two transitions. A careful look at Fig. 3b discloses that the mismatch in the dopant cationic size reduces the T_c .

The decrease in phase transition temperature has also been observed by Kimura and Greenblatt [10] in the case of trivalent cation doped Li_2SO_4 . Similarly, Murray and Secco [11] have noted the lowering of the phase transition temperature in potassium doped Na_2SO_4 . Irvine and West [12] have explained the decrease in T_c by assuming that the substitution of the alio-valent dopant cation results in the creation of extrinsic vacancies which causes an intrinsic disorder. According to them, the order–disorder transition occurs more readily with rising temperature and T_c is displaced to a lower temperature. However, our earlier studies in iso-valent doped systems strongly indicate that even in the absence of extrinsic vacancies the T_c can be lowered [7, 13]. This lowering of T_c is understood to be due to localized lattice distortion taking place on account of size mismatch. The lattice distortion imparts additional strain energy to the lattice relative to that of the pure host which is considered as a main factor in promoting the orthorhombic (β) to hexagonal (α) phase transition at low temperatures. For $x \geq 5.27$, the transition temperature stays around 409°C , thus indicating the separation of the phases. The decrease in the value of ΔH corresponding to $x \geq 5.27$ (Fig. 3a) strongly supports the above conclusion. The XRD, DSC and SEM results are complementary to each other which set the solid solubility limit of alio-valent cations in Ag_2SO_4 at 5.27 mole% (corresponding to 5% vacancy). Interestingly, Ca^{2+} and Ba^{2+} doped samples anomalously fall out of the regular trend with drastically low values of ΔH associated with these systems.

2.4 Infrared spectroscopy (IR)

Tables 4, 5 show the fundamental frequencies of SO_4^{2-} having T_d symmetry occurring at ν_1, ν_2, ν_3 and ν_4 (respectively, the symmetric stretching (Raman active), doubly degenerate bending (IR active) and the doubly degenerate antisymmetric

Table 4. IR data of $(100-x)\text{Ag}_2\text{SO}_4 : (x)\text{Me}_2\text{SO}_4$

	Ag_2SO_4	Me = Li		Me = Na		Me = Rb	
$x =$	0.0	0.5	1.0	3.0	0.5	1.0	3.0
ν_1	983	980	980	981	984	987	989
ν_2	466	467	482	485	471	472	468
ν_3	1123	1121	1116	1121	1125	1127	1128
ν_4	619	617	617	618	618	617	620

All frequencies are in cm^{-1}

Table 5. IR data of $(100-x)\text{Ag}_2\text{SO}_4 : (x)(\text{M}'_2\text{SO}_4)_3$

	Ag_2SO_4				$\text{M}' = \text{Dy}$				$\text{M}' = \text{Gd}$				$\text{M}' = \text{Sm}$				$\text{M}' = \text{La}$			
$x =$	0.00	1.50	2.56	3.63	1.50	2.56	3.63	1.50	2.56	3.63	1.50	2.56	3.63	1.50	2.56	3.63	1.50	2.56	3.63	
ν_1	983	988	988	988	990	992	992	992	986	986	987	984	984	984	984	984	984	984	984	984
ν_2	466	470	470	470	470	470	470	470	470	470	470	467	467	471	467	467	471	467	467	471
ν_3	1123	1125	1128	1129	1123	1128	1128	1129	1122	1125	1126	1114	1114	1112	1114	1114	1112	1114	1114	1112
ν_4	619	617	617	616	617	618	617	618	617	618	617	617	617	617	617	617	617	617	617	617

All frequencies are in cm^{-1}

(IR and Raman active frequencies)). Various frequencies obtained from the infrared spectra of a number of compositions including that of pure Ag_2SO_4 are compared with the standard spectra of Ag_2SO_4 in Tables 4, 5 to understand the role played by the impurity cation *vis-a-vis* the Ag_2SO_4 structure. Other than these peaks, the additional peaks in each spectrum at different frequencies are assigned as a combination of fundamental frequencies. As seen, ν_1 and ν_3 shift to the lower values when the Ag^+ is replaced by Li^+ ($r_g < r_h$). On the other hand, the shifts corresponding to ν_1 and ν_3 are towards the higher value when the host ion is replaced by a larger cation like Rb^+ .

Energy considerations (mainly electrostatic and thermodynamic) suggest the splitting of degenerate modes which depends on cations; it increases with increase in ionic radii, ionic polarizability and cation oxygen distance for isomorphous sulphates. As seen in Tables 4, 5 no other additional frequencies other than those corresponding to Ag_2SO_4 are present. This rules out the possibility of precipitation or formation of an intermediate phase. These results strongly support the XRD results (Tables 1, 2) and the confirmation of the solid solution limits.

This study has clearly demonstrated the influence of lattice distortion on the environment of SO_4^{2-} which leads to the shift in vibrational frequencies. The appearance of some modified peaks is thus attributed to a change in S–O distance. These modifications support the concept of lattice distortion which influences the mobility of the mobile ion in the lattice. Interestingly, a careful look at Tables 4, 5 suggests the stretching of ν_1 and ν_3 towards higher values for substitution of trivalent cations ($r_g < r_h$) in contrast to those given for the substitution of monovalent cations in the Ag_2SO_4 matrix.

2.5 Impedance analysis

The results of complex impedance spectroscopy are critically analysed to find bulk properties by eliminating extraneous parameters such as electrode polarization and grain boundary. A distorted semicircular arc is observed for the pure sample (Fig. 4). A closer look at this figure reveals that the distorted semicircular arc is a combination of two overlapping depressed semicircular arcs. On the other hand, a single semicircular arc is seen for K^+ , Rb^+ and Cs^+ and the divalent cation doped Ag_2SO_4 which is attributed to the limitation of the upper sweep frequency (13 MHz). However, there are two discernible semicircular arcs in the case of the rest of the samples. Since the conductive silver coating on both the surfaces of the electrolyte acts as a reversible (non-blocking) electrode, no electrode polarization is reflected in the complex impedance plane. A non-linear least squares (NLS) fit method

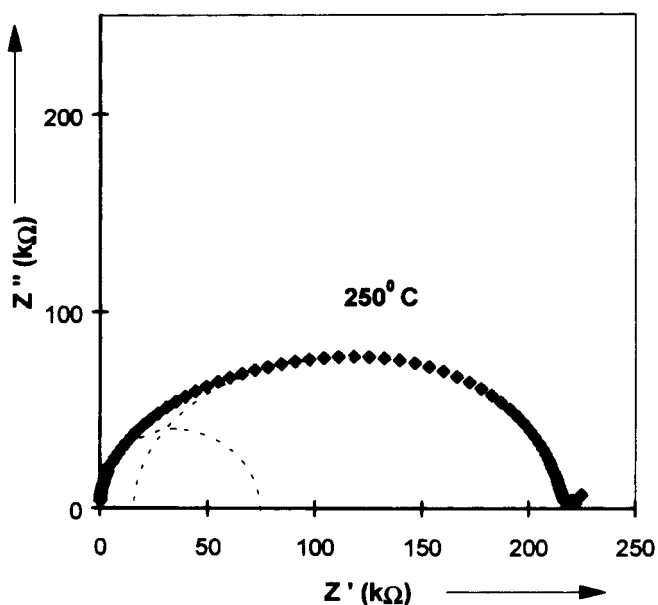


Fig. 4. Complex impedance plot for pure Ag_2SO_4 at 250°C (the full line represents the best fit curve)

is used to ascertain the presence of two overlapping depressed semicircular arcs. In order to accomplish this, the complex impedance data acquired at a fixed temperature using a computer controlled HP 4192A IF impedance analyser is fitted to the equation:

$$Z(\omega) = Z(0) + \frac{Z(\infty) - Z(0)}{1 + (j\omega\tau)^\alpha} \quad (1)$$

where the symbols carry their usual meaning [14], using our software developed in *Turbo C*. During the NLS fitting the sum of squares is minimized by unity weighting represented by

$$S_i = [(\Delta R_i)^2 + (\Delta I_i)^2]^{1/2} \quad (2)$$

where ΔR_i and ΔI_i are the real and imaginary fitting residuals. Table 6 presents impedance data. The presence of two overlapping depressed semicircular arcs is suggestive of the occurrence of two prominent conduction mechanisms simultaneously under the external perturbation ac signal. Various interpretations can be made in the impedance analysis in a polycrystalline ion conducting specimen; however, an experimental impedance obviously contains major contributions from intergrain and intragrain ion migration [15, 16]. In order to have a more meaningful discussion, the voluminous

impedance data obtained by following the above procedure are presented in concise form (Table 6) using the equation

$$f_p = f_0 \exp(-E_m/kT). \quad (3)$$

The peak frequency of the complex impedance $\omega_{\max} = 2\pi f_p$ is given by $1/\tau$, and

$$\frac{1}{\tau} = \frac{1}{RC} = \frac{\sigma}{\varepsilon\alpha\mu C}, \quad \mu = \mu_0 \exp(-E_m/kT) \quad (4)$$

where μ is the cationic mobility, E_m denotes the migration enthalpy, μ_0 is proportional to the jump attempt frequency, and k and T are the Boltzmann constant and temperature in K. The frequency f_p derived from ω_{\max} is an effective averaged hopping frequency of an ion. The effective prefactor f_0 depends on the defect charge carrier density, C .

The process of ion migration through the sample involves the activation energy (Table 6) for migration of ions across the grain boundaries, E_{a2} (obtained from the semicircle corresponding to high frequency) and that for intragrain ion migration, E_{a1} (obtained from the semicircle corresponding to low frequency). Evidently, the partial replacement of the host Ag^+ by dopant cations within the grain alters the local environment leaving the grain boundary undisturbed. This alteration in the local environment modifies the activation enthalpy for intragrain ion migration, whereas that for intergrain conduction remains invariant. Similar results are found in case of the iso-valent cation doped Li_2SO_4 [7].

2.6 Ionic conductivity

Arrhenius plots for all the compositions are found to obey the Arrhenius law (5) in both the α and β phases (as an example, Fig. 5 depicts this behaviour for the host Ag_2SO_4).

$$(\sigma T) = (\sigma T)_0 \exp(-E_a/kT). \quad (5)$$

The observed change in slope at 416°C with an order of magnitude jump in conductivity in the case of pure Ag_2SO_4 accounts for the orthorhombic (β) to hexagonal (α) phase transition (Fig. 5). The magnitudes of the conductivities ($2.22 \times 10^{-5} \text{ S cm}^{-1}$ at 250°C and $3.4 \times 10^{-3} \text{ S cm}^{-1}$ at

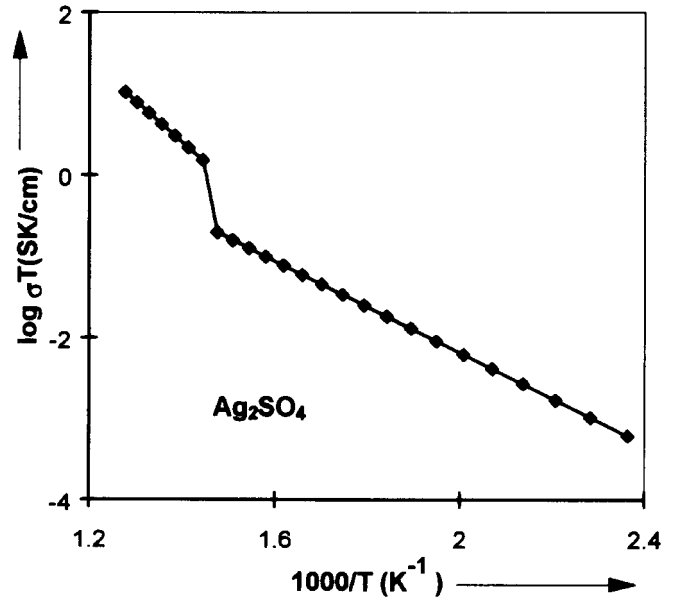


Fig. 5. Variation of $\log(\sigma T)$ with $10^3/T$ for pure Ag_2SO_4

440°C) and the transition temperature (416°C) are in close agreement with earlier reports [17–19].

2.6.1 Isovalent cation doped Ag_2SO_4 .

As seen in Figs. 6a and b, the conductivity is optimized in the β - and α -phases for $x = 3$ mole% in the case of Li, K, and Rb doping, whereas the conductivity is found to decrease slightly with concentration for Na doped Ag_2SO_4 . The Cs^+ doping decreases the conductivity in β - Ag_2SO_4 . A closer look at the figure clearly reveals that the Rb^+ doped sample gives the maximum conductivity in both phases. Interestingly, the Li^+ doped samples have conductivities comparable to that of the pure host system. When Ag^+ is partially substituted by Me^+ , a lattice distortion (increased entropy) occurs, in general, affecting the mobility of the cation in the host lattice. Particularly, a localized lattice contraction takes place if $r_g < r_h$ (such as Na^+ and Li^+ replacing Ag^+), and the lattice expands if $r_g > r_h$ (such as K^+ , Rb^+ or Cs^+ replacing Ag^+) as substantiated by the experimental facts (Table 3).

Table 6. Impedance data of some samples

System	$R_{b1}(\text{Ohm})$	Low freq. corresponding				High freq. corresponding				
		α_1	$f_{p1}(\text{kHz})$	$\log f_{p01}(\text{kHz})$	$E_{a1}(\text{eV})$	$R_{b2}(\text{Ohm})$	α_2	$f_{p2}(\text{kHz})$	$\log f_{p02}(\text{kHz})$	$E_{a2}(\text{eV})$
Me = Li, x=0.000	2010	0.930	8952	12.142	0.610	2079	0.850	10010	11.68	0.550
Me = Li, x=3.333	3523	0.999	6865	10.244	0.409	8111	0.999	6919	12.727	0.346
Me = Na, x=3.351	5334	0.999	3723	10.304	0.462	93	0.999	3121	12.417	0.485
Me = K, x=3.330	2344	0.999	5535	11.006	0.509	–	–	–	–	–
Me = Rb, x=3.312	960	0.999	10523	10.596	0.414	–	–	–	–	–
Me = Cs, x=3.332	5417	0.999	3426	15.800	1.111	–	–	–	–	–
$M' = \text{La}$, x=3.630	1037	0.93	10796	11.620	0.550	–	–	–	11.538	0.515
$M' = \text{Gd}$, x=3.630	260.17	0.999	11210	11.310	0.521	213.71	0.997	11713	11.321	0.52
$M' = \text{Y}$, x=3.630	1111.4	0.792	12863	11.700	0.535	913.00	0.790	–	11.55	0.515
$M' = \text{Dy}$, x=3.630	1696.7	0.927	1357	11.001	0.577	1393.8	0.925	–	11.79	0.535
$M' = \text{Sm}$, x=3.630	1208.8	0.929	3545	10.980	0.533	993.02	0.927	4635.6	11.005	0.522

– Insufficient data due to limitation of upper sweep frequency

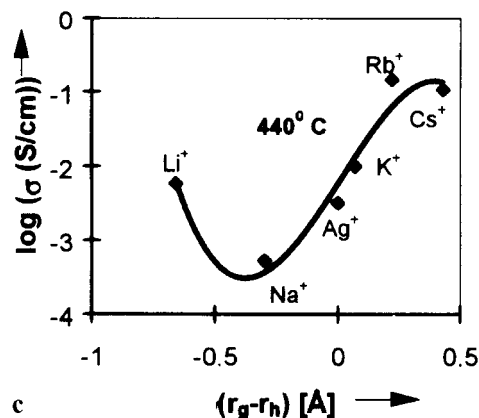
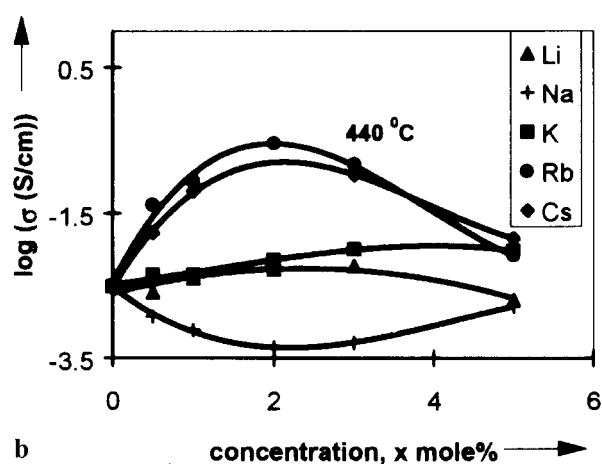
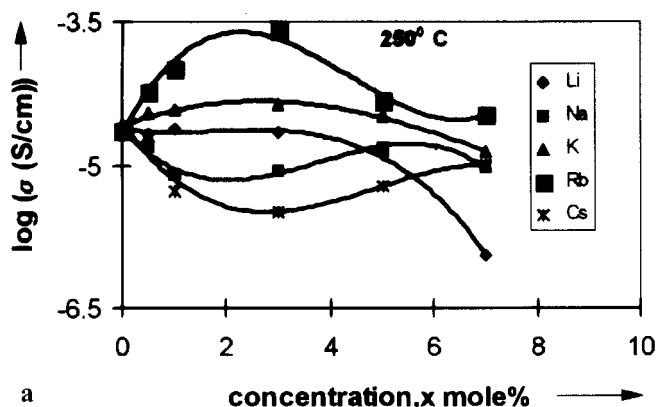


Fig. 6. Variation of $\log(\sigma)$ with x for $(100-x)\text{Ag}_2\text{SO}_4 : (x)\text{Me}_2\text{SO}_4$ [Me = Li, K and Rb] at (a) 250 °C, (b) 440 °C and (c) with distortion factor $(r_g - r_h)$ for $x = 3$ at 250 °C

The concentration of mobile charge carriers in a Frenkel type ionic solid is given by

$$n = (k_f)^{1/2} \exp[(\Delta S_{\text{th}} + \Delta S_{\text{cf}})/2k] \exp(-E_f/kT) \quad (6)$$

where k_f , ΔS_{th} , ΔS_{cf} and E_f are, respectively, the mass action constant, thermal entropy, configurational entropy and defect formation enthalpy. If the system under consideration (solid solution of Ag_2SO_4 with Me_2SO_4) is assumed to be homo-

geneous and isotropic, then the term ΔS_{cf} remains invariant with respect to the distribution of cations and anions, whereas the immediate ions surrounding Me^+ will have a different vibrational frequency (ν') from those at regular undistorted sites (ν). The thermal entropy term, ΔS_{th} , in (6) will be a consequence of the change in frequency of the lattice vibration due to the distortion taking place. Considering the Einstein model [20] we may assume that in the doped crystal, each atom neighbouring Me^+ is equivalent to three harmonic oscillators each of frequency $\nu' \neq \nu$. Then one finds for the increase in thermal entropy per M^+ the expression,

$$\Delta S_{\text{th}} = 12k \log(\nu/\nu'), \quad (7)$$

substitution of which in (6) leads to:

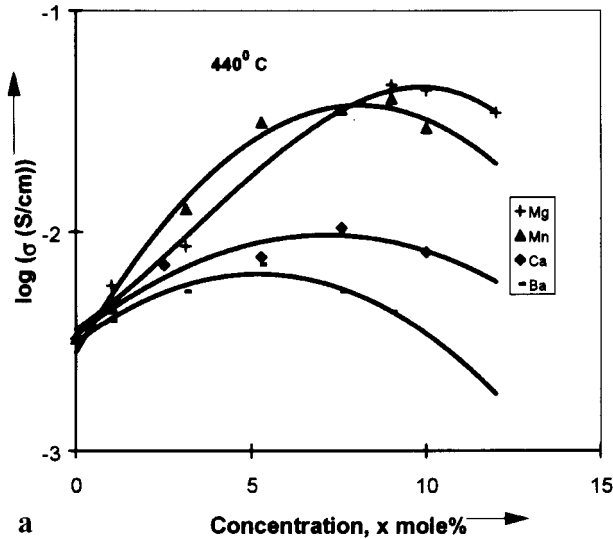
$$n = (k_f)(\nu/\nu')^6 \exp(-E_f/2kT). \quad (8)$$

If the cation replacing Ag^+ is such that $r_g < r_h$, then the lattice contraction takes place and $\nu' > \nu$. This reduces the mobile charge carrier (Ag^+) concentration, n . This is reflected in the conductivity behaviour (a decrease in conductivity) in the cases of Na^+ and Li^+ doped samples (Fig. 6c). The opposite behaviour is expected if $r_g > r_h$ in which case lattice loosening occurs. Such an expansion opens the lattice in the vicinity of Me^+ thereby widening the window (opening) between the two energetically equivalent cationic sites through which the ion undergoes successive jumps from an occupied site to the vacant site. Cs^+ has $r_g \gg r_h$ such that the lattice undergoes expansion but beyond a critical value of $(r_g - r_h) \sim 0.21 \text{ \AA}$, the wrong-sized dopant ion hinders the mobility of Ag^+ , thus reducing the conductivity (Fig. 6c). Nevertheless, in the case of Li_2SO_4 added to Ag_2SO_4 , in spite of the lattice contraction the lattice opening of the host is large enough for the added Li^+ that it itself can move from one site to a nearby vacant site, i.e., the added Li^+ becomes the mobile charge carrier.

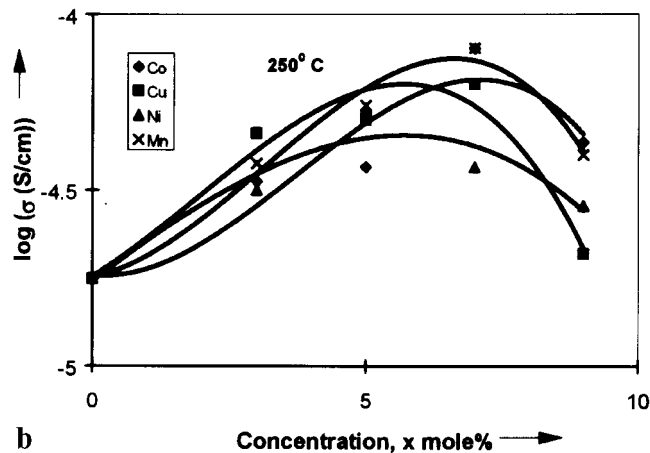
Additionally, coupling [21] of $\text{Ag}^+ - \text{Li}^+$ helps in the enhancement of the conductivity; the net effect is such that in spite of the lattice contraction, in the case of Li^+ doped Ag_2SO_4 , the conductivity is marginally enhanced. The observed insignificant decrease in conductivity (Na^+ doped Ag_2SO_4) is understandable because with the addition of Na^+ the total mobile charge carrier density remains the same. A small decrease in conductivity due to partial replacement of Ag^+ by Na^+ has also been observed by Secco et al. [22].

2.6.2 Alio-valent cation doped Ag_2SO_4 .

Divalent cation doped Ag_2SO_4 . Figures 7a, b show the variation of conductivity with concentration for M^{2+} doped Ag_2SO_4 in α - and β -phases, respectively. The conductivity is seen to be optimized nearly at 5.27 mole% in the α -phase, corresponding to 5% vacancy. Clearly, the conductivity of all the doped samples is seen (Fig. 7a) to be greater than that of the host (Ag_2SO_4). Strikingly, with the exception of Mg^{2+} doping, no dependence of conductivity on the lattice distortion factor $(r_g - r_h)$ is seen. Figure 8a depicts the conductivity variation of various divalent doped samples (at 5% vacancy, solid soluble) with respect to the distortion factor $(r_g - r_h)$ in the β -phase. It is worth noting that the conductivity of the Ba^{2+} doped sample and those belonging to the transition metal (d-group elements) doped Ag_2SO_4 is seen to have increased as



a



b

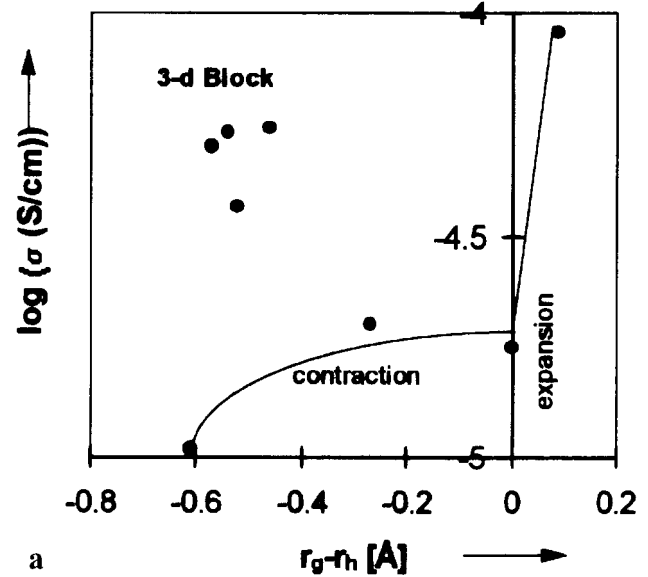
Fig. 7. Variation of $\log(\sigma)$ of the $(100-x)\text{Ag}_2\text{SO}_4 : (x)\text{MSO}_4$ system with concentration in (a) the α -phase, and (b) the β -phase

compared to that of the pure sample. On the other hand, the conductivity of Mg^{2+} and Ca^{2+} doped Ag_2SO_4 is seen to have decreased. Figure 8b, representing the variation of activation energy as a function of the distortion factor, reveals that the activation energy of the Ba^{2+} doped sample is lower than that of the host (in agreement with the conductivity behaviour), whereas the transition metal cation doped samples have higher activation energy, in contrast to their conductivity behaviour as depicted in Fig. 7. The results pertaining to alkaline earth metal cation doped β - Ag_2SO_4 can be understood in the light of our theory on lattice contraction/expansion [7].

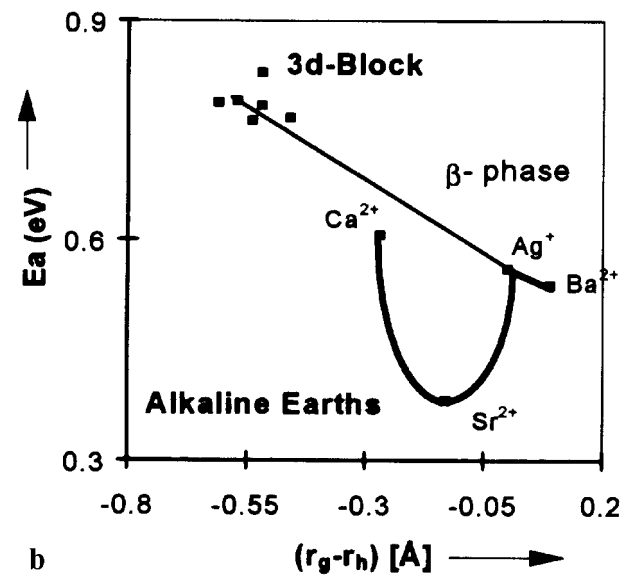
The partial replacement of the host monovalent by the guest divalent M^{2+} gives rise to additional extrinsic cationic vacancies so as to attain thermodynamic equilibria (constancy of the electrochemical potential, constancy of the activity, and hence constancy of the electrical potential) in the host lattice as per the formula:



In addition to the creation of an extrinsic vacancy in the vicinity of M^{2+} , expansion/contraction of the host lattice takes



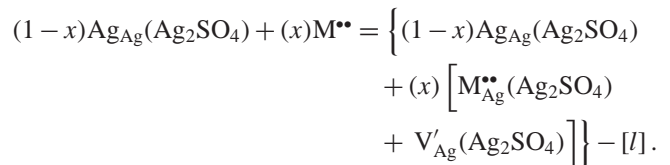
a



b

Fig. 8. Variation of (a) $\log(\sigma)$ at 250°C , and (b) E_a with distortion factor $(r_g - r_h)$ for $(94.73)\text{Ag}_2\text{SO}_4 : (5.27)\text{MSO}_4$ in the β -phase

place if $r_g > r_h$ or $r_g < r_h$. The disorder reaction can be written using the Kroger-Vink notation as:



In the high-temperature phase, extrinsic vacancies contribute chiefly to the conductivity, whereas the ionic size effect is inconsequential following alio-valent dopant substitution in the host sublattice. Further, the hexagonal phase being a more open structure, Ag^+ ions squeeze through the lattice with a high elementary hopping probability on account of the availability of additional vacancies created by MSO_4 substitu-

tion. With the increase in vacancy concentration due to partial substitution of M^{2+} , an additional migration path for Ag^+ is created which in turn increases the conductivity (Fig. 7). Upon further addition beyond $x = 5.27$ mole% (5% vacancy) the mobility of Ag^+ is reduced following vacancy–vacancy interaction such as cluster formation and also cationic sublattice ordering [5]. In sharp contrast to the results of alkaline earth cation doped systems (Fig. 8a), the conductivity is seen to be more than that of the host for transition element doped Ag_2SO_4 in the low-temperature region. This conductivity behaviour in these systems is anomalous, particularly in the light of the fact that a transition element cation has a smaller ionic radius than that of Ag^+ giving lattice contraction.

The electronic configuration and the polarizability of the dopant cation in Ag_2SO_4 -based systems seems to play an important role. The polarizability of the ion is related to the deformability of its electron cloud. However, the usual assumption of dependence of the polarizable ion on the net ionic charge *vis-à-vis* its size is invalid in respect of metal cations having d electrons which shield the nucleus poorly. That is, two ions of the same charge and approximate size, one with a noble gas configuration, such as Mg^{2+} , will be less polarizing than the one with d^x (such as Mn^{2+}) configuration (Table 7). This important factor has to be taken into consideration so far as the bonding properties of the activated mobile cation and SO_4^{2-} framework is concerned. Starting with the assumption of having a soft electrostatic/covalent interactions involving Ag^+ , Mn^{2+} or Co^{2+} with SO_4^{2-} , the weaker bonding between d^x ions and the SO_4^{2-} is expected to permit a greater ease of mobility for the ions thus accounting for the high cationic conductivity.

Also, it has been suggested [23] that the quadrupolar polarizability of mobile metal ions should reduce the energy barrier associated with the motion along mobile ion pathways from the minima at the site of high symmetry to the energy barrier at the site of lower symmetry.

The mobile Ag^+ may acquire a larger mobility when it is made to pass through the potential contours surrounding the '3-d-block' dopant cations, thus leading to higher conductivity in spite of the lattice contraction taking place. Additionally, the mobile M^{2+} may contribute to the conductivity owing to a number of extrinsic vacancies available because of substitution of Ag^+ by such a dopant ion in the Ag_2SO_4 matrix. In contrast, this important factor of polarizability is absent when the dopant ion belongs to the s-block of which Mg^{2+} and Ca^{2+} are the members.

Trivalent cation doped Ag_2SO_4 . Figures 9a and b show the variation of conductivity of M^{3+} doped Ag_2SO_4 with concentration in α - and β -phases. The conductivity is seen to be optimized nearly at 2.56 mole% (corresponding to 5% vacancy). As seen, the conductivity of all the doped samples is greater than that of the host (Figs. 9a and b), the Gd^{3+} doped sample giving the maximum enhancement in conductivity. Interestingly, in contrast with the results of d-block dopants, the trivalent cation doped Ag_2SO_4 has a lower activation energy than that of the pure substance. Conforming to the formula



there are two additional extrinsic vacancies for the mobile Ag^+ in the close vicinity of the impurity (M^{3+}) which par-

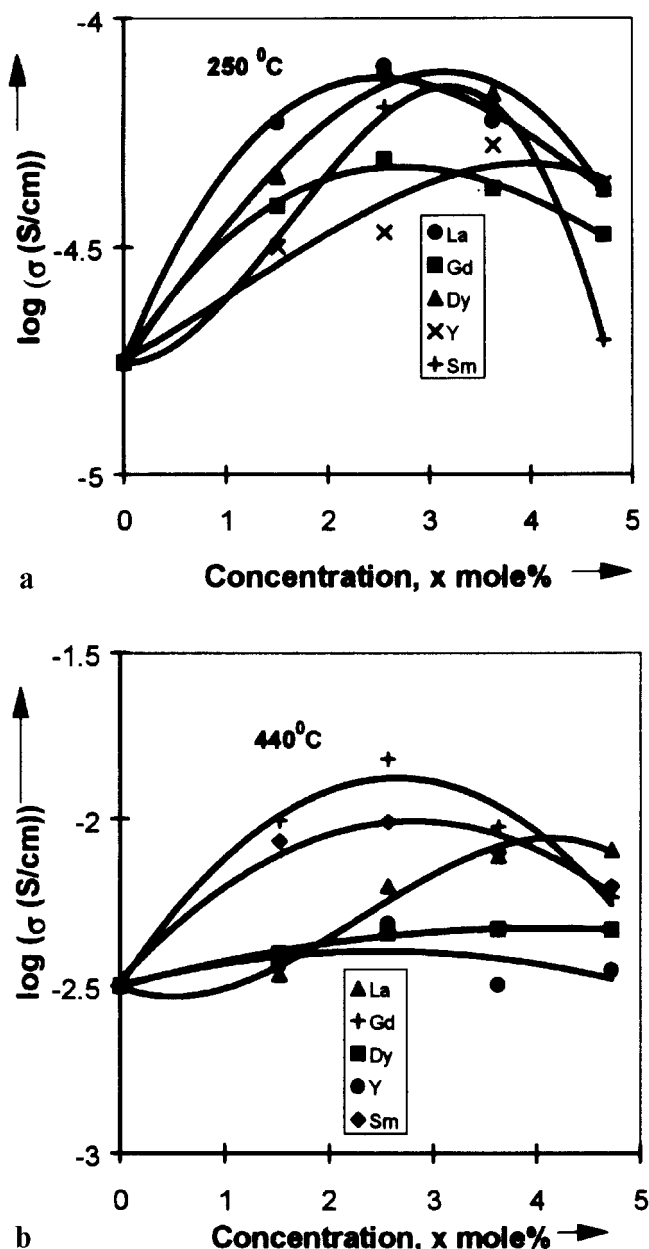


Fig. 9. Variation of $\log(\sigma)$ with concentration for $(100-x)Ag_2SO_4 : (x)(M_2SO_4)_3$ at (a) 250 °C and (b) 440 °C

tially replaces Ag^+ in the host lattice. On the other hand, since M^{3+} has a lower ionic radius than Ag^+ , this substitution facilitates localized lattice contraction (Tables 4, 5). Nevertheless, a large ionic conductivity in these samples is attributed to: (i) the availability of additional extrinsic vacancies to the mobile Ag^+ as discussed above, and (ii) the presence of half or completely filled d and f shells (Table 7) of the dopants contributes to the polarizability.

The relative enhancement in conductivity, $\Delta\sigma_r$ ($\Delta\sigma_r = \sigma_h/\sigma_g$), for different dopants (iso- and alio-valent) at 250 and 440 °C for maximum conductivity is displayed in Table 8. Evidently, more effective enhancement in conductivity is achieved in the low-temperature β -phase than that in the high-temperature α -phase. In the latter case, there exists a large number of intrinsic cation percolating paths, obviously due

Table 7. Electronic configuration, ionic radius, distortion factor, polarizability and structure of some mono-, di- and trivalent sulphates studied

Sr. No.	Cation	Electronic configuration	ionic radius (Å)	Distortion factor (Å)	polarizability	Structure of sulphate at 27 °C
1	Li	1s ² , 2s ¹	0.60	-0.66	1.0	monoclinic
2	Na	[Ne]3s ¹	0.96	-0.3	0.9	orthorhombic
3	Ag	[Kr]4d ¹⁰ , 5s ¹	1.26	0.00	1.9	orthorhombic
4	K	[Ar]4s ¹	1.33	0.07	0.8	orthorhombic
5	Rb	[Kr]5s ¹	1.48	0.22	0.8	orthorhombic
6	Cs	[Xe]6s ¹	1.69	0.43	0.7	–
7	Co	[Ar]3d ⁷ , 4s ²	0.74	-0.52	1.8	orthorhombic
8	Ni	[Ar]3d ⁸ , 4s ²	0.72	-0.54	1.8	orthorhombic
9	Mn	[Ar]3d ⁵ , 4s ²	0.80	-0.46	1.5	orthorhombic
10	Zn	[Ar]3d ¹⁰ , 4s ²	0.74	-0.52	1.6	orthorhombic
11	Cu	[Ar]3d ¹⁰ , 4s ¹	0.69	-0.57	1.9	orthorhombic
12	Ca	[Ar]4s ²	0.99	-0.27	1.0	orthorhombic
13	Mg	[Ne]3s ²	0.65	-0.61	1.2	orthorhombic
14	Ba	[Xe]5s ²	1.35	0.09	0.9	orthorhombic
15	Sr	[Ar]5s ²	1.13	-0.13	1.0	orthorhombic
16	Pb	[Xe]4f ¹⁴ , 5d ¹⁰ , 6s ² , 6p ²	1.20	-0.06	1.3	orthorhombic
17	Gd	[Xe]4f ⁷ , 5d ¹ , 6s ²	1.02	-0.24	1.1	–
18	Dy	[Xe]4f ¹⁰ , 5d ¹ , 6s ²	0.99	-0.27	–	rhombohedral
19	Y	[Kr]4d ¹ , 5s ²	0.91	-0.35	1.3	rhombohedral
20	Sm	[Xe]4f ⁶ , 5d ¹ , 6s ²	1.02	-0.24	1.2	–
21	La	[Xe]5d ¹ , 6s ²	1.15	-0.11	1.1	–

Table 8. The relative enhancement in conductivity, $\Delta\sigma_r$ ($\Delta\sigma_r = \sigma_h/\sigma_g$) for different dopants (iso- and alio-valent) at 250 and 440 °C for maximum conductivity giving samples

System	log σ (S/cm) at 440 °C	log σ (S/cm) at 250 °C	σ_h/σ_g at 440 °C	σ_h/σ_g at 250 °C
Ag ₂ SO ₄ , pure	-2.499	-4.753	1.000	1.000
Me = Li	-2.228	-4.542	0.535	0.616
Me = Na	-3.284	-4.942	6.092	1.547
Me = K	-2.001	-4.257	0.317	0.319
Me = Rb	-0.839	-3.474	0.022	0.052
Me = Cs	-0.975	-5.400	0.030	4.443
M = Co	-1.570	-4.434	0.117	0.479
M = Ni	-1.657	-4.269	0.144	0.328
M = Mn	-1.504	-4.260	0.101	3.321
M = Zn	-1.837	-4.385	0.217	0.430
M = Cu	-2.012	-4.300	0.325	0.352
M = Ca	-2.115	-4.698	0.412	0.882
M = Mg	-2.066	-4.983	0.369	1.700
M = Ba	-2.150	-4.046	0.447	0.196
M = Sr	-2.436	-4.304	0.864	0.356
M = Pb	-2.039	-4.700	0.346	0.384
M' = Gd	-1.820	-4.106	0.208	0.225
M' = Dy	-2.343	-4.308	0.698	0.359
M' = Y	-2.315	-4.111	0.653	0.228
M' = Sm	-2.008	-4.468	0.323	0.519
M' = La	-2.202	-4.195	0.505	0.276

to its more open structure and built-in excessive defect concentration, and therefore the net effect of impurity addition is less significant. On the other hand, the various characteristics associated with the dopant ion, viz., ionic size, valence and electronic structure of the guest cation, play a vital role in governing the conductivity in β -Ag₂SO₄.

3 Conclusion

The ionic conductivity is found to increase with the incorporation of a guest cation of *appropriate* distortion factor, $r_g - r_h$, in both iso- and alio-valent cation doped Ag₂SO₄. The increase in conductivity in the transition element cation doped Ag₂SO₄, despite having $r_g < r_h$, is due to the probable role played by the polarizability. The conductivity of Ag₂SO₄ is found to be dependent on the ionic size, the va-

lence and the electronic structure of the guest cation, particularly in the low-temperature modification of Ag₂SO₄ (β -phase). It is found, generally, to be invariant with respect to these factors in α -Ag₂SO₄. These results could throw light on the fundamental conduction mechanism in Ag₂SO₄ and also on the criterion of selecting the impurity cation in the classical doping method. The optimized solid electrolytes can then be utilized for their technological applications in electrochemical devices such as SO_x sensors and thermal batteries.

Acknowledgements. The authors are grateful to CSIR, New Delhi, for providing financial assistance. The authors are also grateful to Prof. Roger Frech, Department of Chemistry and Biochemistry, University of Oklahoma, USA for his useful guidance and suggestions in carrying out the present work.

References

1. M. Gauthier, A. Chamberland: *J. Electrochem. Soc.* **124**, 1579 (1977)
2. Q.G. Liu, W.L. Worrell: U.S. Patent Applic. p.17, **303–320** (Sep.17, 1981)
3. W.L. Worrell, Q.G. Liu: *J. Electroanal. Chem.* **168**, 355 (1984)
4. M. Mari, M. Beghi, S. Pizzini: *Sensors and Actuators B*, **2**, 51 (1990)
5. H.H. Hofer, W. Eysel, U.V. Alpen: *J. Solid State Chem.* **36**, 365 (1981)
6. K. Singh, S.S. Bhoga: *Solid State Ionics*, **39**, 205 (1990)
7. K. Singh, S.S. Bhoga, S.W. Anwane: *J. Appl. Phy.* (in press)
8. K. Singh, S.S. Bhoga, S.W. Anwane: *Solid State Ionics*, 1996 (in press)
9. K. Singh: *Solid State Ionics*, **28**, 1371 (1988)
10. N. Kimura, M. Greenblatt: *Mater. Res. Bull.* **19**, 1653 (1984)
11. R.M. Murray, E.A. Secco: *Can. J. Chem.* **56**, 2616 (1978)
12. J.T.S. Irvine, A.R. West: *Solid State Ionics*, **28**, 214 (1988)
13. K. Singh, S.S. Bhoga: *J. Solid State Chem.* **97**, 141 (1992)
14. K. Singh, U.K. Lanje, S.S. Bhoga: *Solid State Ionics* (1996) (in press)
15. K. Singh: *Solid State Ionics*, **66**, 5 (1993)
16. S.H. Chu, M.A. Seitz: *J. Solid State Chem.*, **23**, 297 (1987)
17. Q.G. Liu, W.L. Worrell: *Solid State Ionics*, **18**, 524 (1986)
18. Q. Liu, X. Sun, W. Wu: *Solid State Ionics*, **40**, 456 (1990)
19. Y. Lu, E.A. Secco, M.G. Usha: *J. Phys. Chem. Solids*, **54**, 821 (1993)
20. E. Medelung: *Physik. Z.* **11**, 898 (1910)
21. H. Øye: Thesis, Technical University of Norway, Trondheim (1963)
22. E.A. Secco, M.G. Usha: *Solid State Ionics*, **68**, 213 (1994)
23. W.G. Kleppmann, H. Blitz: *Comm. Phys.* **1**, 105 (1976)